Journal Pre-proof

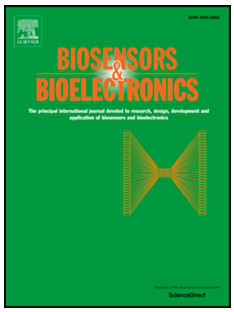

Bimetallic nanoparticles decorated hollow nanoporous carbon framework as nanozyme biosensor for highly sensitive electrochemical sensing of uric acid

Kaidong Wang, Can Wu, Feng Wang, Minghao Liao, Guoqiang Jiang

PII: S0956-5663(19)30948-0

DOI: https://doi.org/10.1016/j.bios.2019.111869

Reference: BIOS 111869

To appear in: *Biosensors and Bioelectronics*

Received Date: 31 July 2019

Revised Date: 8 November 2019

Accepted Date: 8 November 2019

Please cite this article as: Wang, K., Wu, C., Wang, F., Liao, M., Jiang, G., Bimetallic nanoparticles decorated hollow nanoporous carbon framework as nanozyme biosensor for highly sensitive electrochemical sensing of uric acid, *Biosensors and Bioelectronics* (2019), doi: https://doi.org/10.1016/j.bios.2019.111869.

Bimetallic nanoparticles decorated hollow nanoporous carbon framework as nanozyme biosensor for highly sensitive electrochemical sensing of uric acid

Kaidong Wang[a], Can Wu[b], Feng Wang[c], Minghao Liao[a], Guoqiang Jiang[a,*]

[a]*Key Laboratory for Industrial Biocatalysis, Ministry of Education, Department of Chemical Engineering, Tsinghua University, Beijing 100084, China*

[b]*School of Materials Science & Engineering, Hubei University, Wuhan 430062, China*

[c]*Department of Chemistry, Key Laboratory of Bioorganic Phosphorus Chemistry & Chemical Biology Beijing Key Laboratory for Analytical Methods and Instrumentation, Tsinghua University, Beijing 100084, China*

*Corresponding author.

E-mail address: jianggq@tsinghua.edu.cn (G. Jiang).

Phone: +86-01062782824.

ABSTRACT

An ultrasensitive electrochemical biosensor was developed to identify the low levels of uric acid (UA) in human serum. The gold/cobalt (Au/Co) bimetallic nanoparticles (NPs) decorated hollow nanoporous carbon framework (Au/Co@HNCF) was synthesized as a nanozyme by pyrolysis of the Au (III)-etching zeolitic imidazolate framework-67 (ZIF-67). The external Au NPs combined with internal Co NPs on the hollow carbon framework exhibited enhanced activity for UA oxidation, thereby generating superior signals. Accordingly, the Au/Co@HNCF biosensor presented ranking performances with a low detection limit of 0.023 μM (S/N = 3), an ultrahigh sensitivity of 48.4 μA μM^{-1} cm^{-2}, and an extensive response in the linear region of 0.1–25 μM and the logarithmic region of 25–2500 μM. Owing to the ordered nanoporous framework and carbon interfacial features, the Au/Co@HNCF biosensor displayed adequate selectivity for UA sensing over a series of biomolecules. In addition, the Au/Co@HNCF biosensor was employed to quantify UA in human serum samples. The test results were basically consistent with those of a commercial apparatus, and thus demonstrated that the proposed Au/Co@HNCF biosensor was reliable for UA determination in clinical research.

Keywords: Electrochemical biosensor; Uric acid; Nanozyme; Bimetallic nanoparticles; Hollow nanoporous carbon

1. Introduction

Uric acid (UA; 2,6,8-trihydroxypurine), as the ultimate metabolite of purine nucleotides, is released by the kidneys into human fluids (Jain et al., 2019). The regular window of UA in healthy human serum is generally 120–460 μM (Liu et al., 2017a). The excess value of UA is used as a momentous biomarker for many clinical diseases, such as uarthritis, nephrosis, and cardiovascular diseases (Shahamirifard et al., 2018). Recent research suggests that the below normal UA level is an important indicator of neuropapillitis, neurodegenerative diseases, sclerosis, and aplastic anemia (Lu et al., 2019; Nigam and Bush, 2019; Long et al., 2016), thus letting determination of the low UA concentrations in human fluids become a crucial challenge. Electrochemical biosensors have many characteristics, such as high accuracy, easy operation, miniaturized devices, which are regarded as the desired devices for UA monitoring (Sha et al., 2019). Nevertheless, the current electrochemical biosensors are insufficient for determination of UA at a low level. Hence, building an ultrasensitive electrochemical biosensor for UA monitoring is highly imperative.

Nanozymes, the nanomaterials with enzyme-mimetic activity, hold tremendous promise for a variety of applications, such as electrochemical sensors, catalysis, and energy conversion (Huang et al., 2019; Cai et al., 2019; Xu et al., 2018). As the substitutions to biological enzymes, nanozymes have inherent superiorities, such as high activity, strong stability (Wang et al., 2018a). Although the great breakthroughs by taking advantage of some nanozymes have been made in the fabrication of highly efficient electrochemical biosensors (Cai et al., 2019; Xu et al., 2018; Li et al., 2019; Tian et al., 2018), constructing more innovative nanozymes is highly desired. Currently, one of the prevalent problems in designing nanozymes is that the substrate can directly and casually diffuse into active sites, which leads to weak selectivity (Wu et al., 2019).

Nanozyme electrochemical biosensors need to have a highly conductive architecture with discriminative features (Maduraiveeran et al., 2018). Hence, a facile assembly of active sites and suitable architectures is a great challenge to be tackled. Metal-organic frameworks (MOFs) present ordered cavity, high metal ion contents, adjustable chemical properties, and are becoming the prospective precursors to construct porous metal-carbon hybrids (Hu et al., 2015).

For enzymatic electrochemical biosensors, the direct electron transfer (DET) between active sites of enzymes and electrode is mainly explored by adjusting the favorable enzyme orientation on electrically

conductive vehicles (Lee et al., 2019; Nguyen et al., 2019). However, enzymatic electrochemical biosensors still have major limitations, such as high cost, poor stability. In this study, we explore the use of ultrafine gold/cobalt (Au/Co) nanoparticles (NPs) decorated hollow nanoporous carbon framework (Au/Co@HNCF) as a nanozyme to fabricate UA electrochemical biosensor. The Au/Co@HNCF is constructed by pyrolysis of the Au (III)-etching zeolitic imidazolate framework-67 (ZIF-67). Considering that recent studies reveal a low UA concentration is interrelated with more variety of diseases, it is vital to build a highly selective UA electrochemical biosensor that has a lower detection limit.

2. Experimental

2.1. Reagents

Cobalt (II) nitrate hexahydrate, 2-methylimidazole (2-MeIm), uric acid (UA), L-serine (Ser), L-asparagine (Asp), ascorbic acid (AA), urea, glycine (Gly), L-histidine (His), glucose (Glu), dopamine (DA), N-methylpyrrolidinone (NMP), and polyvinylidene fluoride (PVDF) were purchased from J&K Chemical Reagent Company (Beijing, China). $HAuCl_4$ solution (23.5–23.8 wt% Au) was obtained from Aladdin (Shanghai, China).

2.2. Synthesis of Au (III)-etching ZIF-67

The synthesis routes of ZIF-67 are presented in the supplementary materials. Afterwards, the ZIF-67 (50 mg) was dispersed in 25 mL of methanol solution then sonicated for 10 min. Then, $HAuCl_4$ solution (5 μL) was added into the above solution. Next, the solution was stirred vehemently for 1 h. After that, the precursor (Au (III)-etching ZIF-67) was gathered by centrifugal separation, washing, and vacuum drying at 70 °C for 24 h.

2.3. Synthesis of Au/Co@HNCF

The precursor (80 mg) was pyrolyzed at 900 °C for 2 h with a heating rate of 5 °C min^{-1} in argon. The black powder (Au/Co NPs decorated hollow nanoporous carbon framework, expressed as Au/Co@HNCF) was obtained after cooling down to room temperature. The ZIF-67 underwent a similar procedure, and the

obtained product (Co NPs decorated nanoporous carbon framework) was expressed as Co@NCF.

2.4. Material characterizations

Detailed descriptions are presented in the supplementary materials.

2.5. Electrochemical studies

The pyrolytic powder (4 mg) was dispersed in 1 mL NMP solution containing 0.4 mg PVDF, then sonicated for 3 h. Afterwards, 5 μL of the dispersed solution was dropped onto the cleaned surface of a glassy carbon electrode (GCE; 3 mm in diameter), then vacuum dried at 50 °C for 12 h. Human serum samples were obtained from the Department of Rheumatology at Qi Lu Hospital of Shangdong University in China. The test results of UA concentrations in human serum samples using the Au/Co@HNCF biosensor were compared with those using the Roche Diagnostics Cobas® 8000 analysis system. Further details about the electrochemical experiments are provided in the supplementary materials.

3. Results and discussion

3.1. Synthesis routes

The two-step synthesis routes for Au/Co@HNCF are presented in Fig. S1. In the first step, the Au (III) ions act as more powerful electron acceptors, thereby producing stronger coordination interactions with 2-MeIm. The etching processes proceed on the surfaces of ZIF-67 tendentiously. Thus, the core-shell architectures are acquired. In the second step, the Au (III)-etching ZIF-67 precursor is pyrolyzed into Au/Co@HNCF. The organic ligand (2-MeIm) acts as the reducing agent and carbon source during the pyrolysis process. The Au (III) and Co (II) ions are reduced into Au/Co NPs by 2-MeIm, meanwhile, the organic ligand is pyrolyzed into the hollow nanoporous carbon framework. The Au (III)-etching effects would weaken the coordination bonds between Co (II) ions and 2-MeIm. The tensions during the pyrolysis process would cause the core collapse, thus leading to form hollow nanoporous carbon framework (Liu et al., 2018; Indra et al., 2018).

3.2. Structural and morphological characterizations

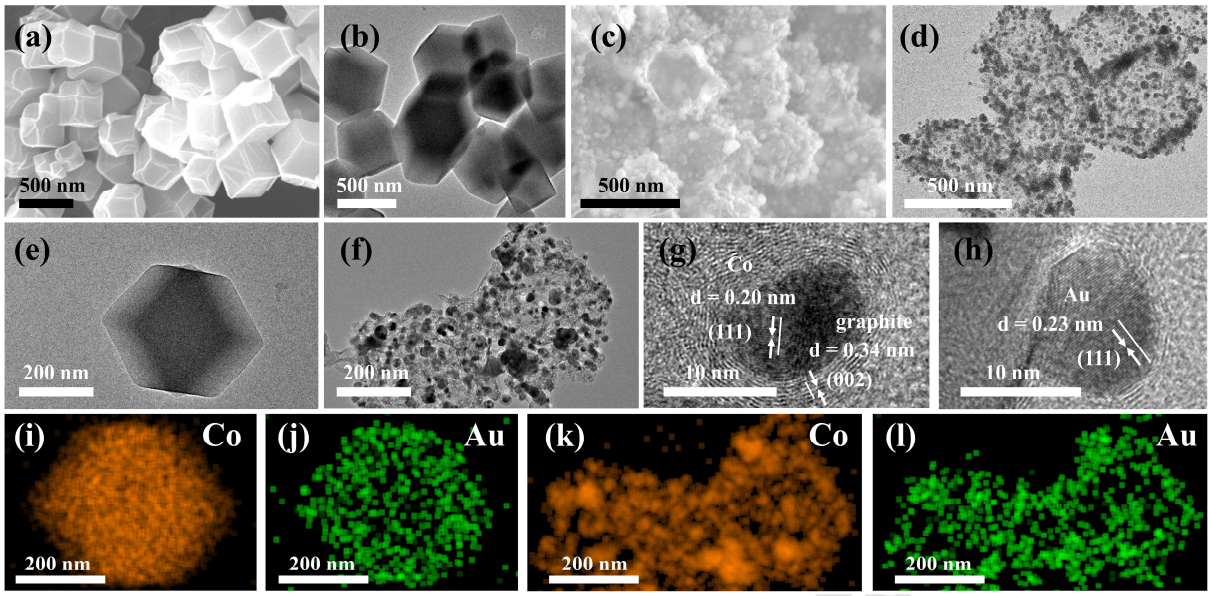

Fig. 1. SEM (a) and TEM (b, e) images of Au (III)-etching ZIF-67; SEM (c) and TEM (d, f) images of Au/Co@HNCF; (g, h) HRTEM images of graphite, Co NPs, and Au NPs; EDX elemental maps of Co (i) and Au (j) species on Au (III)-etching ZIF-67, Co (k) and Au (l) species on Au/Co@HNCF.

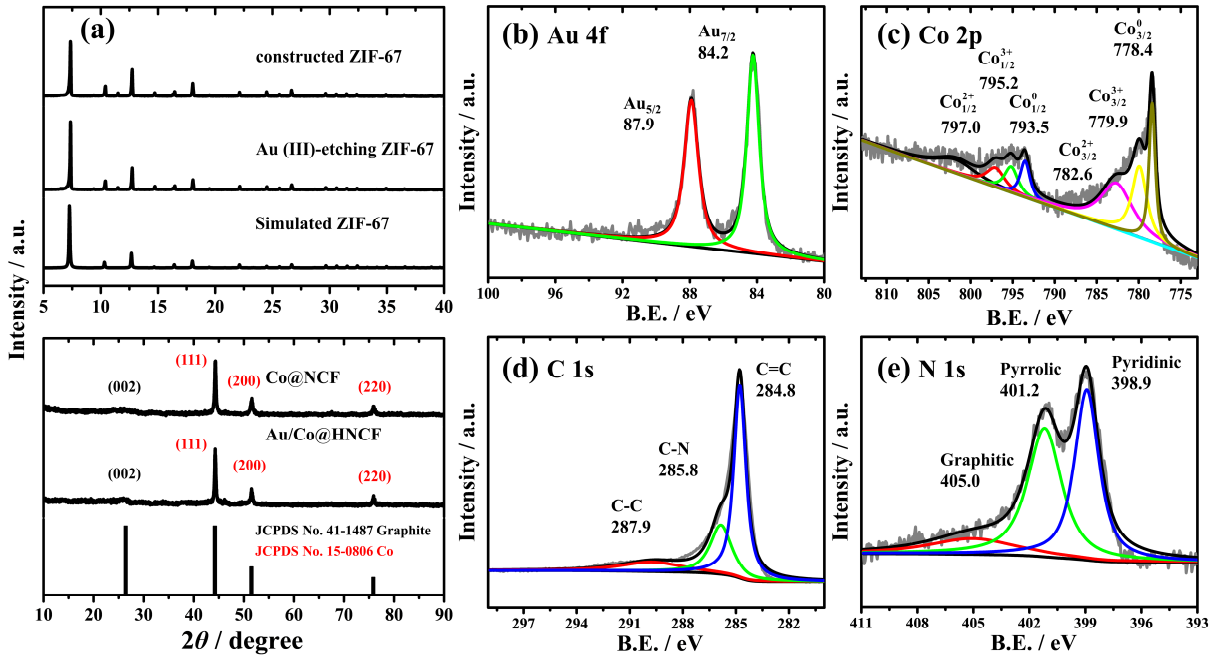

Fig. 2. (a) XRD patterns of constructed ZIF-67, Au (III)-etching ZIF-67, simulated ZIF-67, Co@NCF, and Au/Co@HNCF; XPS spectra of (b) Au 4f, (c) Co 2p, (d) C 1s, and (e) N 1s regions.

To build the Au/Co@HNCF, the Au (III)-etching ZIF-67 was initially constructed. Scanning electron microscopy (SEM) images showed that the Au (III)-etching ZIF-67 was dodecahedrons (Fig. 1a).

Transmission electron microscopy (TEM) revealed that the morphologies of the solid dodecahedrons were maintained after the etching procedure (Fig. 1b, 1e, and S2). The X-ray diffraction (XRD) tests were implemented to discern the diffraction peaks (Fig. 2a). The primary XRD peaks of the constructed ZIF-67 and the Au (III)-etching ZIF-67 were found to be in accordance with those of the simulated ZIF-67 (Wang et al., 2018b), which implied that the Au (III)-etching ZIF-67 maintained the crystal structures. The energy-dispersive X-ray (EDX) elemental maps confirmed the core-shell architectures and determined the chemical compositions of inner core and outer shell (Fig. 1i and 1j). The intensities of Au species at the outer regions were stronger than those at the inner regions (Fig. 1j), which implied that the Au (III)-etching procedure was effective for synthesizing the core-shell bimetallic precursor.

Next, a pyrolysis procedure was implemented to turn the precursor into Au/Co@HNCF. Interestingly, the hollow architectures were constructed after the pyrolysis of Au (III)-etching ZIF-67 (Fig. 1c, 1d, and 1f). The constructed Au/Co@HNCF displayed ultrafine NPs decorated hollow dodecahedrons. The high-resolution TEM (HRTEM) was implemented to recognize the compositions of pyrolytic product. The *d*-spacing fringes of 0.34 nm, 0.20 nm, and 0.23 nm corresponded to the (002) plane of graphite (Fig. 1g), the (111) plane of Co NPs (Fig. 1g), and the (111) plane of Au NPs (Fig. 1h) (Wang et al., 2018c; Bai et al., 2018), respectively. The EDX elemental images showed that Co NPs and Au NPs were decorated uniformly on the internal layer (Fig. 1k) and the outer layer (Fig. 1l), respectively, thus validating the reliable construction of Au/Co NPs bimetallic decorated hollow architectures.

In addition, X-ray photoelectron spectroscopy (XPS) tests were implemented to probe the valence states of Au/Co@HNCF (Fig. 2b, 2c, 2d, and 2e) (Wang et al., 2018d). The Au 4f spectrum appeared one pair of peaks (Au $4f_{5/2}/4f_{7/2}$) at 87.9 and 84.2 eV, which were assigned to Au^0 (Fig. 2b) (Kumar et al., 2018). Three groups of peaks (Co $2p_{1/2}/2p_{3/2}$) at 793.5/778.4, 797.0/782.6, and 795.2/779.9 were identified for the Co 2p spectrum, which could correspond to Co^0, Co^{2+}, and Co^{3+} (Fig. 2c). In Fig. 2d, the peaks at 287.9, 285.8, and 284.8 eV were assigned to C-C, C-N, and C=C. The N 1s spectrum appeared three peaks at 405.0, 401.2, and 398.9 eV, indicating the presence of graphitic-N, pyrrolic-N, and pyridinic-N (Fig. 2e). Consistently, XPS results verified that the Au/Co NPs decorated carbon framework had been effectively synthesized. Moreover, Raman analysis suggested that the Au/Co@HNCF contained both the disordered (D-band) and graphitic carbon (G-band) (Fig. S3).

3.3. Electrochemical properties

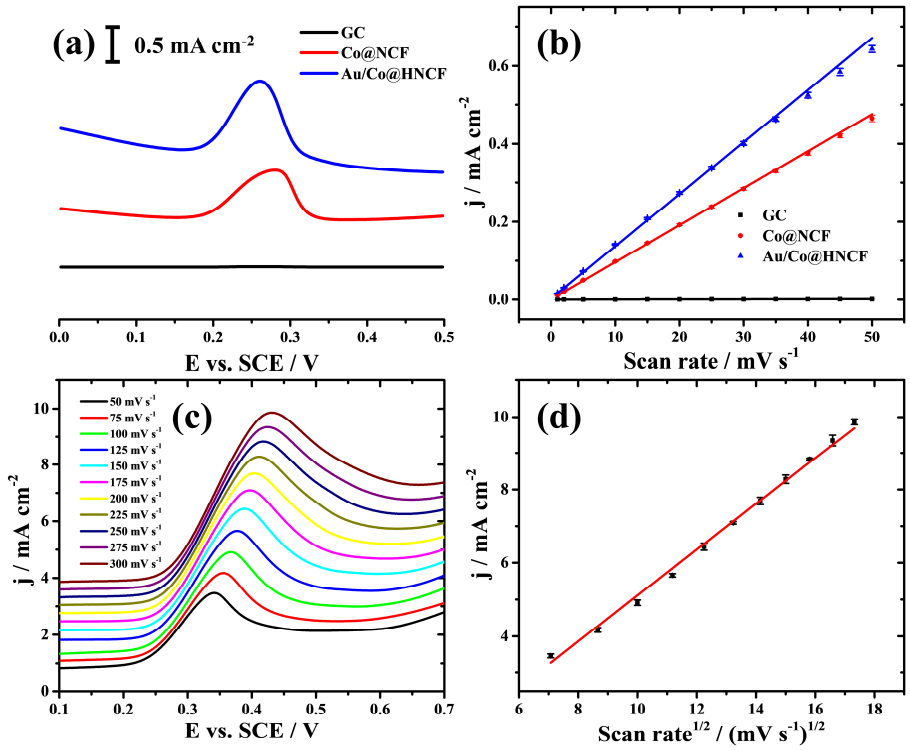

Fig. 3. (a) DPV curves for GC, fabricated Co@NCF and Au/Co@HNCF biosensor; (b) Linear fitting for capacitive j at 0.3 V (vs. SCE) versus scan rate; (c) LSV curves at different scan rates; (d) Corresponding linear fitting for j_p versus the square root of scan rate ($v^{1/2}$). Error bars represent the standard deviations of five tests. (RSD ≤ 3.3%, n = 5)

The pH effects on electro-oxidation of UA (25 μM) were studied by differential pulse voltammetry (DPV) (Fig. S4 and S5). The peak current density (j_p) increased with rising pH until pH 7.4. Then, the DPV responses decreased promptly (Fig. S5a and S5b). Explanatorily, along with pH increasing, the UA molecules become dissociated slightly, thereby leading to the enhanced sensing signals. Nevertheless, completely deprotonated UA molecules (anionic forms) would be excluded from the electron-rich electrode surfaces with pH rising unceasingly, thus resulting in decrease in DPV signals (Shahamirifard et al., 2018; Matsoso et al., 2019). Consequently, the PBS (pH 7.4) was selected as the electrolyte solution for the following tests. The peak potential (E_p) decreased with pH rising (Fig. S5a and Fig. S5c). The slope of linear fitting was 63 mV/pH (Fig. S5c), implying the approximately identical numbers of electrons and protons in the UA oxidation (Li et al., 2018). The electrochemical oxidation reaction of UA (Reaction 1)

was presented in Fig. S6 (Feng et al., 2019; Sha et al., 2019). The electrochemical oxidation mechanism of UA on the Au/Co@HNCF biosensor was proposed. In the whole processes, the Au/Co NPs act as catalytic sites for the electrochemical oxidation of UA (Sha et al., 2019; Matsoso et al., 2019; Zhao et al., 2016; Kim et al., 2017; Fester et al., 2018; Wang et al., 2016). In the first step, the Au/Co NPs in Au/Co@HNCF are electrochemically oxidized and release electrons into the electrode. Therefore, the current signals for UA sensing are generated. In the second step, the oxidative Au/Co NPs chemically oxidize UA (Reaction 1, Fig. S6), meanwhile, the Co/Au NPs in oxidative status recover to their initial status.

The DPV responses of the Co@NCF and Au/Co@HNCF biosensors for UA (25 μM) oxidation were compared. As described in Fig. 3a, the Au/Co@HNCF biosensor exhibited 1.49-fold higher j_p for UA oxidation than the Co@NCF biosensor did. A negatively shifted E_p (~ 20 mV) was observed using the Au/Co@HNCF biosensor for UA oxidation, indicating the improved electron-transfer kinetics (Zhang et al., 2018). Possibly, the bimetallic NPs decorated carbon framework could offer preferable bonding sites and behave higher activity for the catalytic dissociation of UA molecules (Ciampi et al., 2018). The electrochemically active surface area (ECSA) was calculated to delve into the electrochemical properties of the fabricated biosensors (Fig. 3b and S7). The Au/Co@HNCF biosensor (7.88 cm^2) exhibited significantly higher ECSA than the bare GC electrode (0.0155 cm^2) did, which indicated the existence of abundant active sites on the Au/Co@HNCF modified layers. The Au/Co@HNCF biosensor possessed higher ECSA (1.41-fold; 7.88 cm^2) than the Co@NCF biosensor (5.58 cm^{-2}) did, which suggested that the Au/Co@HNCF biosensor had a greater number of active sites. In addition, the effects of scan rates on UA oxidation using the Au/Co@HNCF biosensor were studied by linear sweep voltammetry (LSV). The j_p increased linearly with $v^{1/2}$, which implied that the UA electro-oxidation was diffusion-confined (Fig. 3c and 3d) (Maduraiveeran et al., 2018; Kumar et al., 2008; Wang et al., 2018b).

In order to ascertain the interfacial properties, the electrochemical impedance spectroscopy (EIS) tests were implemented (Fig. S8) (An et al., 2018; Gu et al., 2018). The smaller semicircles on Nyquist plots of the Co@NCF and Au/Co@HNCF biosensors showed that the charge-transfer resistance (R_{ct}) was decreased after being coated, implying the enhanced conductivity and the faster charge-transfer rate. The steeper linear segments on Nyquist plots of Au/Co@HNCF biosensor compared to that of Co@NCF biosensor implied the faster mass-transport rate of Au/Co@HNCF biosensor towards redox couples (Fig. S8b). The shorter mass-transport routes of hollow architectures were beneficial to improve the

diffusion-confined reactions, which further demonstrated the vital role of the Au (III)-etching procedure in fabricating the Au/Co@HNCF biosensor (Yu et al., 2017). Additionally, the average pore diameter was determined by nitrogen adsorption/desorption analysis (Fig. S9). The average pore diameter of Au/Co@HNCF (2.2 nm) was found to be larger than that of Co@NCF (0.96 nm). The dilated pore diameter could expose a larger number of active sites (Zhu et al., 2016; Remi et al., 2016; Liu et al., 2017b). The electro-oxidation reaction of UA was diffusion-controlled (Fig. 3c and 3d) (Maduraiveeran et al., 2018; Kumar et al., 2008; Wang et al., 2018b). The dilated pore diameter can not only lead to an increased number of accessible active sites, but also promote UA diffusion and transport (Zhu et al., 2016; Remi et al., 2016; Liu et al., 2017b), thereby contributing to enhanced electro-catalytic oxidation of UA. Jointly, the Au/Co@HNCF possessed highly active Au/Co NPs, adequate active sites, highly conductive framework, and dilated pore diameter, as a result, presenting the faster electron-transfer rate and mass-transport rate.

3.4. Electrochemical determination

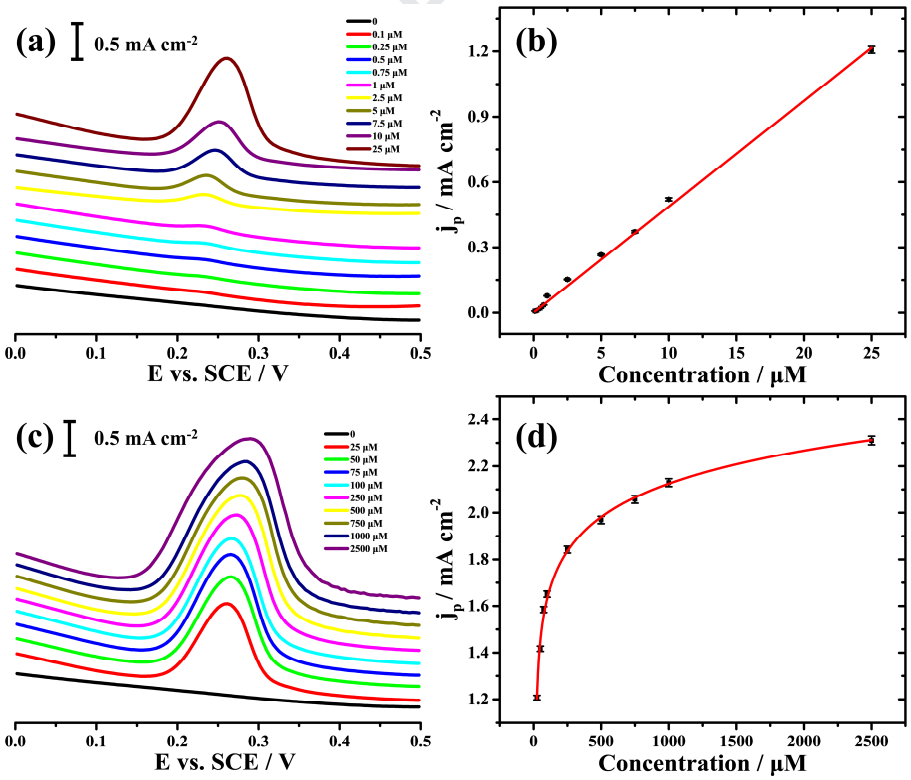

Fig. 4. DPV curves and corresponding calibration curves for j_p versus C_{UA} in the range of (a, b) 0.1–25 μM and (c, d) 25–2500 μM. (RSD ≤ 2.7%, n = 5)

The DPV method was implemented to study the correlation between j_p (mA cm^{-2}) and uric acid concentration (C_{UA}) in the range of 0.1–2500 μM (Fig. 4). The j_p increased linearly in the range of 0.1–25 μM (Fig. 4a). The linear equation was $j_{p1} = 0.0484 \times C_{UA1} + 0.011$ (Fig. 4b). The sensitivity was 48.4 μA μM^{-1} cm^{-2}. The limit of detection (LOD) was 0.023 μM (S/N = 3). With C_{UA} rising in the range of 25–2500 μM, the j_p went up logarithmically (Fig. 4c). The logarithmic equation was $j_{p2} = 0.202 \times ln\ (C_{UA2} - 14.619) + 0.731$. At higher concentrations (25–2500 μM), the active sites of Au/Co@HNCF for oxidizing UA molecules approached to saturation (Prasad and Fatma, 2017; Kumar et al., 2008). Therefore, the j_p increased logarithmically with C_{UA} increasing. Emphatically, the performances of the Au/Co@HNCF biosensor for UA determination preceded the performances of other electrochemical biosensors (Table S1).

3.5. Selectivity, reproducibility, and stability

The typical test methods were employed to ascertain the current responses for UA determination in presence of different interfering biomolecules (Guan et al., 2014; Si et al., 2018; Ozcan and Sahin, 2010). The experimental concentrations of biomolecules and the normal ranges in human serum were shown in Table S2. The prepared solutions containing UA and different interfering biomolecules were diluted 12 times by 0.1 M PBS (pH 7.4) before they were analyzed (Guan et al., 2014; Si et al., 2018; Ozcan and Sahin, 2010). The final concentration of UA was 10 μM after dilution. The test results were presented in Fig. 5 and Fig. S10. The DPV responses varied in 95.1–104.4 % (n = 5) (Fig. 5 and S10), which indicated that the Au/Co@HNCF biosensor had prominent selectivity for UA determination. The AA and DA are small biomolecules. There are some similarities in molecular structures between UA and AA or DA. The AA or DA would competitively occupy some active sites during the anti-interference experiments (Yang et al., 2016; Zhang et al., 2018; Wu et al., 2015). As a result, the DPV signal for UA determination was depressed when ascorbic acid or dopamine were added. The intra-day and inter-day (six consecutive days) reproducibility of the Au/Co@HNCF biosensor were assessed using six independent Au/Co@HNCF biosensors under identically fabricated conditions for UA (25 μM) determination. The relative standard deviation (RSD) values of intra-day and inter-day reproducibility were 4.1% and 4.3%, respectively, which indicated the reliable reproducibility of this developed biosensor. Furthermore, the stability was assessed by determining the DPV responses towards 25 μM UA over the following 30 days. The DPV responses were retained above 90.7% of the initial responses after 30 days (Fig. S11), which demonstrated the all-right

stability of the fabricated Au/Co@HNCF biosensor.

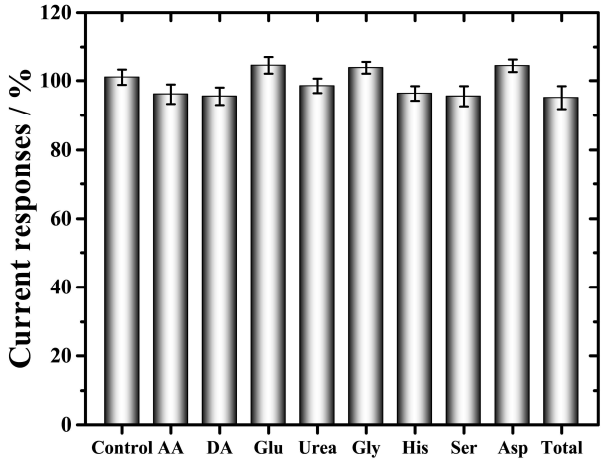

Fig. 5. DPV responses for UA determination over different interfering biomolecules using the Au/Co@HNCF biosensor (the experimental concentrations of these biomolecules were shown in Table S2). (RSD ≤ 3.3%, n = 5)

3.6. Real samples analysis

The feasibility of the Au/Co@HNCF biosensor for UA determination in real samples was evaluated using 10 human serum samples. First, the human serum samples were diluted 100 times by PBS (pH 7.4) (Guan et al., 2014; Si et al., 2018; Ozcan and Sahin, 2010). Then, DPV signals for UA determination were recorded. Finally, the C_{UA} was calculated quantitatively. The comparison for test results using the Au/Co@HNCF biosensor and the Roche Diagnostics Cobas® 8000 analysis system was presented in Table 1. The normal window of UA in healthy human serum is 120–460 μM (Liu et al., 2017a). The C_{UA} in human serum samples 7 and 8 exceeded the normal range slightly, which implied the possible hyperuricemia, and this was associated with hypertension, metabolic syndrome, and cardiovascular diseases. The comparative percentage variations (%) of the C_{UAa} (measured uric acid concentration using the Au/Co@HNCF biosensor) and the C_{UAb} (measured uric acid concentration using the Roche Diagnostics Cobas® 8000 analysis system) were found to range from 91.8% to 107.5% based on the calculated equation: Percentage Variation (%) = $C_{UAa}/C_{UAb} \times 100\%$. The test results using the Au/Co@HNCF biosensor were basically consistent with those using the Roche Diagnostics Cobas® 8000 analysis system, which demonstrated that it was feasible and practical to use the Au/Co@HNCF biosensor for UA determination in

clinical research.

Table 1

Comparison for the determination of UA concentration in human serum from the Department of Rheumatology at Hospital using the Au/Co@HNCF biosensor and Roche Diagnostics Cobas® 8000 analysis system. (RSD ≤ 3.9%, n = 5)

Human serum sample	C_{UAa} (μM)	RSD (%, n = 5)	C_{UAb} (μM)	RSD (%, n = 5)	Percentage variation (%)
1	301.1	2.8	328.0	2.9	91.8
2	193.8	1.7	204.3	2.4	94.9
3	125.2	1.1	133.4	1.6	93.9
4	319.2	2.9	304.1	3.6	105.0
5	330.7	3.0	317.8	3.8	104.1
6	225.6	2.1	234.9	2.8	96.0
7	468.2	3.1	488.7	3.9	95.8
8	492.9	2.4	474.2	3.7	103.9
9	371.2	3.2	345.3	2.1	107.5
10	245.1	2.2	237.7	1.9	103.1

3.7. Novelties and perspectives

The study presents a facile strategy for synthesizing the novel Au/Co@HNCF as a nanozyme for UA determination (Indra et al., 2018; Dang et al., 2018). The synthesized Au/Co@HNCF has highly active and abundant catalytic sites as well as ordered and unique nanoporous carbon. Therefore, the fabricated Au/Co@HNCF biosensor for UA determination presents many advantages. First, the Au/Co@HNCF biosensor exhibits a very low detection limit (0.023 μM), which thus could satisfy the clinical requirements for identifying more variety of diseases based on the UA indicator at a low level (Nigam and Bush, 2019; Long et al., 2016). Second, the Au/Co@HNCF biosensor displays a broad detection range (0.1–25; 25–2500 μM). The normal range of UA in healthy human serum is 120–460 μM (Liu et al., 2017a). Both elevated UA levels and reduced UA levels can be detected by the Au/Co@HNCF biosensor (Feng et al.,

2019; Zhang et al., 2018). Generally speaking, the external Au NPs decorated carbon framework would have better biocompatibility (Elahi et al., 2018; Kiew et al., 2016). Therefore, the Au/Co@HNCF biosensor is worthy of being further developed into miniaturized equipment for UA monitoring routinely in biological fluids, if possible, implantable devices. Third, the cost for the synthesis of Au/Co@HNCF (only 0.31 wt% Au) and the fabrication of biosensor is low. The anti-interference abilities, reproducibility, and stability are adequate. With the rapid improvements of living qualities, more variety of UA biosensors based on Au/Co@HNCF, such household apparatus, deserve for being explored. Thus, it is foreseeable that there would be a keen interest for both scholars and engineers to further develop the biosensors based on Au/Co@HNCF for in-situ and point-of-care sensing.

4. Conclusions

In summary, the unique Au/Co@HNCF as a nanozyme has been effectively constructed by pyrolysis of the Au (III)-etching ZIF-67. Benefiting from highly active Au/Co NPs, abundant catalytic sites, and hierarchically ordered porous carbon of Au/Co@HNCF, the fabricated nanozyme electrochemical biosensor for UA determination displays ultrahigh sensitivity and prominent selectivity. Moreover, the Au/Co@HNCF biosensor exhibits a very low detection limit (0.023 μM), which thus could be employed to delve into more variety of diseases, such as neuropapillitis, neurodegenerative diseases, in the clinical research based on a lower UA concentration. However, the further developed biosensors based on Au/Co@HNCF for UA monitoring routinely, such as household apparatus, implantable devices, are still a huge challenge. This work presents a facile strategy for constructing a highly sensitive and selective nanozyme as well as a reliable platform for the further development of electrochemical biosensors.

Declarations of interest: None.

Acknowledgements

This work was supported by the National Natural Science Foundation of China [grant numbers 21576148, 21520102008]. The authors are grateful for the supports from Dr. Qiang Shu in the Department of Rheumatology at Qi Lu Hospital of Shangdong University in China.

References

Jain, S., Verma, S., Singh, S.P., Sharma, S.N., 2019. Biosens. Bioelectron. 127, 135–141.

Liu, Y., Li, H., Guo, B., Wei, L., Chen, B., Zhang, Y., 2017a. Biosens. Bioelectron. 91, 734–740.

Shahamirifard, S.A., Ghaedi, M., Razmi, Z., Hajati, S., 2018. Biosens. Bioelectron. 114, 30–36.

Lu, J., Dalbeth, N., Yin, H., Li, C., Merriman, T.R., Wei, W.H., 2019. Nat. Rev. Rheumatol. 1, 1–14.

Nigam, S.K., Bush, K.T., 2019. Nat. Rev. Nephrol. 15, 301–316.

Long, Q., Fang, A., Wen, Y., Li, H., Zhang, Y., Yao, S., 2016. Biosens. Bioelectron. 86, 109–114.

Sha, R., Vishnu, N., Badhulika, S., 2019. Sens. Actuators B 279, 53–60.

Huang, Y., Ren, J., Qu, X., 2019. Chem. Rev. 119, 4357–4412.

Cai, X., Chen, H., Wang, Z., Sun, W., Shi, L., Zhao, H., Lan, M., 2019. Biosens. Bioelectron. 123, 101–107.

Xu, Q., Yuan, H., Dong, X., Zhang, Y., Asif, M., Dong, Z., He, W., Ren, J., Sun, Y., Xiao, F., 2018. Biosens. Bioelectron. 107, 153–162.

Wang, Q., Wei, H., Zhang, Z., Wang, E., Dong, S., 2018a. Trends Anal. Chem. 105, 218–224.

Li, W., Fan, G.C., Gao, F., Cui, Y., Wang, W., Luo, X., 2019. Biosens. Bioelectron. 127, 64–71.

Tian, L., Qi, J., Oderinde, O., Yao, C., Song, W., Wang, Y., 2018. Biosens. Bioelectron. 110, 110–117.

Wu, J., Wang, X., Wang, Q., Lou, Z., Li, S., Zhu, Y., Qin, L., Wei, H., 2019. Chem. Soc. Rev. 48, 1004–1076.

Maduraiveeran, G., Sasidharan, M., Ganesan, V., 2018. Biosens. Bioelectron. 103, 113–129.

Hu, H., Guan, B., Xia, B., Lou, X.W., 2015. J. Am. Chem. Soc. 137, 5590–5595.

Lee, W.C., Kim, K.B., Gurudatt, N., Hussain, K.K., Choi, C.S., Park, D.S., Shim, Y.B., 2019. Biosens. Bioelectron. 130, 48–54.

Nguyen, T.N., Nolan, J.K., Park, H., Lam, S., Fattah, M., Page, J.C., Joe, H.E., Jun, M.B., Lee, H., Kim, S.J., 2019. Biosens. Bioelectron. 131, 257–266.

Liu, D., Wan, J., Pang, G., Tang, Z., 2018. Adv. Mater. 1803291–1803307.

Indra, A., Song, T., Paik, U., 2018. Adv. Mater. 30, 1705146–17005170.

Wang, K., Wu, C., Wang, F., Jiang, G., 2018b. ACS Appl. Nano Mater. 1, 5843–5853.

Wang, K., Wu, C., Wang, F., Liu, C., Yu, C., Jiang, G., 2018c. Electrochim. Acta 285, 128–138.

Bai, J., Lu, B., Han, Q., Li, Q., Qu, L., 2018. ACS Appl. Mater. Interfaces 10, 38066–38072.

Wang, X.X., Cullen, D.A., Pan, Y.T., Hwang, S., Wang, M., Feng, Z., Wang, J., Engelhard, M.H., Zhang, H.,

He, Y., 2018d. Adv. Mater. 30, 1706758–1706768.

Kumar, G., Tibbitts, L., Newell, J., Panthi, B., Mukhopadhyay, A., Rioux, R.M., Pursell, C.J., Janik, M., Chandler, B.D., 2018. Nat. Chem. 10, 268–274.

Matsoso, B.J., Mutuma, B.K., Billing, C., Ranganathan, K., Lerotholi, T., Jones, G., Coville, N.J., 2019. J. Electroanal. Chem. 833, 160–168.

Li, Q., Huo, C., Yi, K., Zhou, L., Su, L., Hou, X., 2018. Sens. Actuators B 260, 346–356.

Kim, D., Xie, C., Becknell, N., Yu, Y., Karamad, M., Chan, K., Crumlin, E.J., Norskov, J.K., Yang, P., 2017. J. Am. Chem. Soc. 139, 8329–8336.

Fester, J., Makoveev, A., Grumelli, D., Gutzler, R., Sun, Z., Rodriguez-Fernandez, J., Kern, K., Lauritsen, J. V., 2018. Angew. Chem. Int. Ed. 57, 11893–11897.

Wang, J., Cui, W., Liu, Q., Xing, Z., Asiri, A.M., Sun, X., 2016. Adv. Mater. 28, 215–230.

Zhang, W., Liu, L., Li, Y., Wang, D., Ma, H., Ren, H., Shi, Y., Han, Y., Ye, B.C., 2018. Biosens. Bioelectron. 121, 96–103.

Ciampi, S., Darwish, N., Aitken, H.M., Díez-Pérez, I., Coote, M.L., 2018. Chem. Soc. Rev. 47, 5146–5164.

An, G.H., Kim, H., Ahn, H.J., 2018. ACS Appl. Mater. Interfaces 10, 6235–6244.

Gu, M., Choi, J., Lee, T., Park, M., Shin, I.S., Hong, J., Lee, H.W., Kim, B.S., 2018. Nanoscale 10, 16159–16168.

Yu, L., Hu, H., Wu, H.B., Lou, X.W., 2017. Adv. Mater. 29, 1604563–1604601.

Zhu, C., Li, H., Fu, S., Du, D., Lin, Y., 2016. Chem. Soc. Rev. 45, 517–531.

Remi, J.C.S., Lauerer, A., Chmelik, C., Vandendael, I., Terryn, H., Baron, G.V., Denayer, J.F.M., Karger, J., 2016. Nat. Mater. 15, 401–409.

Liu, J., Zhu, D., Guo, C., Vasileff, A., Qiao, S.Z., 2017b. Adv. Energy Mater. 7, 1700518.

Zhao, D., Yu, G., Tian, K., Xu, C., 2016. Biosens. Bioelectron. 82, 119–126.

Prasad, B.B., Fatma, S., 2017. Electrochim. Acta 232, 474–483.

Kumar, S.A., Lo, P.H., Chen, S.M., 2008. Biosens. Bioelectron. 24, 518–523.

Guan, W., Duan, X., Reed, M.A., 2014. Biosens. Bioelectron. 51, 225–231.

Si, Y., Park, J.W., Jung, S., Hwang, G.S., Goh, E., Lee, H.J., 2018. Biosens. Bioelectron. 121, 265–271.

Ozcan, A., Sahin, Y., 2010. Biosens. Bioelectron. 25, 2497–2502.

Yang, L., Ran, X., Cai, L., Li, Y., Zhao, H., Li, C.P., 2016. Biosens. Bioelectron. 83, 347–352.

Wu, C., Sun, H., Li, Y., Liu, X., Du, X., Wang, X., Xu, P., 2015. Biosens. Bioelectron. 66, 350–355.

Dang, S., Zhu, Q.L., Xu, Q., 2018. Nat. Rev. Mater. 3, 17075–17088.

Xiong, C., Zhang, T., Kong, W., Zhang, Z., Qu, H., Chen, W., Wang, Y., Luo, L., Zheng, L., 2018. Biosens. Bioelectron. 101, 21–28.

Ma, L., Zhang, Q., Wu, C., Zhang, Y., Zeng, L., 2019. Anal. Chim. Acta 1055, 17–25.

Feng, J., Li, Q., Cai, J., Yang, T., Chen, J., Hou, X., 2019. Sens. Actuators B 298, 126872–126880.

Elahi, N., Kamali, M., Baghersad, M.H., 2018. Talanta 184, 537–556.

Kiew, S.F., Kiew, L.V., Lee, H.B., Imae, T., Chung, L.Y., 2016. J. Controlled Release 226, 217–228.

Highlights

- Au/Co@HNCF sensor displays ultrahigh sensitivity and prominent selectivity.
- Wide sensing range of 0.1-25 and 25-2500 μM with LOD of 0.023 μM is obtained.
- Unique Au/Co NPs decorated hollow nanoporous carbon framework are prepared.
- Highly active Au/Co NPs and abundant sites result in ultrahigh sensitivity.
- Ordered nanopores and interface discrimination lead to prominent selectivity.

Author Contribution Statement

Kaidong Wang: Methodology; Conceptualization; Carried out experiments; Software; Visualization; Validation; Writing - original draft; Writing - review & editing.

Can Wu: Methodology; Formal analysis; Writing - review & editing.

Feng Wang: Formal analysis; Writing - review & editing.

Minghao Liao: Investigation; Formal analysis; Carried out experiments.

Guoqiang Jiang: Supervision; Formal analysis; Writing - review & editing; Funding acquisition; Project administration.

Declarations of interest: None.

Credit Author Statement

Kaidong Wang: Methodology; Conceptualization; Carried out experiments; Software; Visualization; Validation; Writing - original draft; Writing - review & editing.

Can Wu: Methodology; Formal analysis; Writing - review & editing.

Feng Wang: Formal analysis; Writing - review & editing.

Minghao Liao: Investigation; Formal analysis; Carried out experiments.

Guoqiang Jiang: Supervision; Formal analysis; Writing - review & editing; Funding acquisition; Project administration.

Declaration of interests

☒ The authors declare that they have no known competing financial interests or personal relationships that could have appeared to influence the work reported in this paper.

☐The authors declare the following financial interests/personal relationships which may be considered as potential competing interests: